Preprints (www.preprints.org) | NOT PEER-REVIEWED | Posted: 4 September 2018 doi:10.20944/preprints201809.0064.v1

Peer-reviewed version available at *Minerals* **2018**, *8*, 526; doi:10.3390/min8110526

Trace Metals Distribution in Sulfide Minerals of the Ultramafic-Hosted Hydrothermal Systems: Example from the Kairei Vent Field, Central Indian Ridge

Yejian Wang [a*], Xiqiu Han [a*], Sven Petersen [b], Matthias Frische [b], Zhongyan Qiu [a], Yiyang Cai [a], Peng Zhou [a,c]

[a] Key Laboratory of Submarine Geosciences & Second Institute of Oceanography, State Oceanic Administration, Hangzhou 310012, China

[b]Helmholtz Centre for Ocean Research Kiel (GEOMAR), 24148 Kiel, Germany

[c] College of Marine Geosciences, Ocean University of China, Qingdao 266100, China

E-mail addresses:

yjwang@sio.org.cn (Y. Wang)

xqhan@sio.org.cn (X. Han)

spetersen@geomar.de (S. Petersen)

mfrische@geomar.de (M. Frische)

qiuzy@sio.org.cn (Z. Qiu)

caiyiyang@sio.org.cn (Y. Cai)

pzhou.klsg@sio.org.cn (P. Zhou)

*correponding authors

© 2018 by the author(s). Distributed under a Creative Commons CC BY license.

Preprints (www.preprints.org) | NOT PEER-REVIEWED | Posted: 4 September 2018 doi:10.20944/preprints201809.0064.v1

Peer-reviewed version available at Minerals 2018, 8, 526; doi:10.3390/min8110526

Abstract

The ultramafic-hosted Kairei vent field, located at 25°19′S, 70°02′E towards the northern end of the segment 1 of the Central Indian Ridge (CIR-S1) in a water depth of ~2450 m. This study aims to investigate the distribution of trace elements among sulfides of differing textures, and discuss the possible factors controlling the trace element distribution in those minerals by using LA-ICP-MS spot analyses as well as line scans. Our results show that there are distinct systematic trace element distributions throughout the different minerals：(1) Pyrite is divided into three types at the Kairei, including early-stage euhedral pyrites (py-I), sub-euhedral pyrites (py-II), and colloform pyrites (py-III). Pyrite is generally enriched in Mo, Au, As, Tl, Mn, and U. py-I have higher contents of Se, Te, Bi, and Ni, py-II are enriched in Au relative to py-I and py-III, but poor in Ni, py-III are enriched in Mo, Pb, and U but are poor in Se, Te, Bi, and Au. Variations in the concentrations of Se, Te, and Bi in pyrite are likely governed by the strong temperature gradient. Ni is generally lower than Co in pyrites, indicates that our samples precipitated at a high-temperature condition, whereas the extreme Co enrichment is likely from a magmatic heat source combined serpentinization reactions underlie the deposits. (2) Chalcopyrite is characterized by high concentrations of Co, Se, Te. The abundant of Se and Te in chalcopyrite cause by the high solubilities of Se and Te incorporated into chalcopyrite lattice at high temperature fluids. The concentration of Sb, As and Au is relatively low in chalcopyrite from the Kairei vent field. (3) Sphalerite from both the Zn-rich chimney is characterized by high concentrations of Sn, Co, Ga, Ge, Ag, Pb, Sb, As, and Cd, but depleted in Se, Te, Bi, Mo, Au, Ni, Tl, Mn, Ba, V, and U in comparison with the other minerals. The high concentration of Cd and Co is likely caused by the substitution of Cd^{2+} and Co^{2+} for Zn^{2+} in sphalerite. A high concentration of Pb accompanied by high Ag concentration in sphalerite indicating the Ag occurs in the microinclusions of Pb-bearing minerals such as galena. Au is generally low in sphalerite and strong correlate with Pb suggesting its presence in the microinclusions of galena. The strong correlation of As with Ge in sphalerite from Kairei suggests that they might precipitate under

Preprints (www.preprints.org) | NOT PEER-REVIEWED | Posted: 4 September 2018 doi:10.20944/preprints201809.0064.v1

Peer-reviewed version available at Minerals 2018, 8, 526; doi:10.3390/min8110526

medium- to low-temperature with moderately reduced conditions. (4) Bornite-digenite is very low in most trace elements, except for Co, Se, and Bi. The high concentration of Se and Bi in all the sulfide minerals was observed in bornite-digenite can be explained by abundant Bi-selenide inclusions. Serpentinization in ultramafic-hosted hydrothermal systems might play an important role on Au enrichment in pyrite with low As contents. Compared with felsic-hosted seafloor massive sulfide (SMS) deposits, sulfide minerals from the ultramafic-hosted deposits show higher concentrations of Se and Te, but lower As, Sb, and Au concentrations attributed to the contribution of magmatic volatile input. Significant Se enrichment in chalcopyrite has been found from mafic-hosted SMSs indicate that the primary factor that controls the Se enrichment is its temperature-controlled mobility in fluids.

Keywords: trace elements; hydrothermal sulfides; Laser Ablation ICP-MS; ultramafic-hosted; Central Indian Ridge

Preprints (www.preprints.org) | NOT PEER-REVIEWED | Posted: 4 September 2018 doi:10.20944/preprints201809.0064.v1

Peer-reviewed version available at Minerals 2018, 8, 526; doi:10.3390/min8110526

1. Introduction

Seafloor massive sulfide (SMS) deposits occur at mid-ocean ridges, and also in submarine volcanic arcs and related back-arc basins associated with host rocks of highly variable composition [1]. The geochemical composition of SMS is also highly variable. For example, sulfides from basalt-hosted mid-ocean ridges appear to be depleted in Au, Ag, As, Sb and Pb compared to sulfides from hydrothermal systems in back-arc basins (e.g., [1, 2]). Additionally, sulfide from occurrences associated with ultramafic host rocks at mid-ocean ridges have significantly higher average Au and Cu contents, when compared to the basalt-hosted deposits (e.g., [3-5]). Hence, the geodynamic setting of seafloor hydrothermal systems with its variable host rock compositions represents a first-order control on the geochemical composition of SMS deposits [6].

Sulfide precipitation from hydrothermal fluids which transport metals leached from the host rock, is governed by physical-chemical parameters, such as temperature, salinity, pH, and fO_2-fS_2. Processes such as cooling, boiling, mixing, and fluid-rock interaction are key for sulfide precipitation in hydrothermal systems which could influence those main parameters above [7-9]. Previous studies suggest that recognition of distinct trace element signatures of individual sulfide grains from seafloor hydrothermal systems, can assist with tracking sequences of crystallization and stages of mineralization, sources of metals, and evolution of ore-forming fluids over time in SMS deposits (e.g., [10-12]). Recent work by Wohlgemuth-Ueberwasser et al. (2015) [13], Keith et al. (2016) [8], Melekestseva et al. (2017) [14], and Wang et al. (2017) [15] investigated trace element distributions by using LA-ICP-MS analysis in sulfide minerals from SMS deposits in different geodynamic setting including ultramafic-hosted and basalt-hosted fields as well as a number of fields that are associated with submarine volcanic arcs and back-arc basins. Those studies well-demonstrated that all the parameters mentioned above influence geochemistry and mineralogy and may account for the variable metal enrichment of SMS. There is comparably little data on hydrothermal fields from the Indian Ocean. In a recent publication [4], we focused on the mineralogy and bulk

Preprints (www.preprints.org) | NOT PEER-REVIEWED | Posted: 4 September 2018 doi:10.20944/preprints201809.0064.v1

Peer-reviewed version available at Minerals 2018, 8, 526; doi:10.3390/min8110526

geochemistry of massive sulfides from the Kairei vent field on the Central Indian Ridge, and suggested that the enrichment of Cu, Zn, and trace elements such as Au, Co, and Sn is related to the involvement of ultramafic rocks in the subseafloor thereby strengthening earlier observations from fluid chemistry (hydrogen and methane enrichment) and petrology (sampling of ultramafic rocks to the East of the active vent field). High-resolution geochemical analyses on sulfide minerals are only available for few ultramafic-hosted SMS deposits at mid-ocean ridges. For the Kairei vent field, LA-ICP-MS analyses have been performed on pyrite [8], but there is still little known about the incorporation mechanism of trace elements that are normally enriched in the ultramafic-hosted SMS deposits (e.g., Co, Ni, Sn) in sphalerite and Cu-(Fe)-sulfides.

In the present work, we therefore analyzed major sulfide minerals from the Kairei vent field that come from a wide range of sample types (chimney, massive sulfides, and breccias), for trace elements by using LA-ICP-MS spot analyses as well as line scans. This study aims to investigate the distribution of trace elements among the sulfide minerals, such as pyrite, chalcopyrite, sphalerite, bornite, and covellite of differing textures, and discuss the possible contributing factors (e.g., formation temperature, seawater-fluid mixture, redox) controlling the trace element distribution in those minerals.

2. Geological background

The Kairei vent field is located at 25°19′S, 70°02′E towards the northern end of the segment 1 of the Central Indian Ridge (CIR-S1) in a water depth of ~2450 m (Fig.1; [16]). The Kairei occurs ~1800 m above the rift valley floor on its eastern wall, and is situated >7 km away from the ridge axis. The rift valley wall has a stair step morphology in this region and the active vents occur on the western flank of Hakuho Knoll within a larger area of weathered sulfides (Fig. 1b; [17, 18]). The discharging fluids at the vent field reach temperatures of 365°C, and are characterized by high concentrations of H_2 and CH_4 [17,19], which is comparable to ultramafic-hosted hydrothermal fields along the Mid-Atlantic Ridge (e.g., [20-24]). The outcrops in the vicinity of the Kairei are entirely made up of pillow basalt and sheet flows and no exposures of ultramafic rocks

Preprints (www.preprints.org) | NOT PEER-REVIEWED | Posted: 4 September 2018 doi:10.20944/preprints201809.0064.v1

Peer-reviewed version available at Minerals 2018, 8, 526; doi:10.3390/min8110526

were observed [17-19]. However, there two oceanic core complexes (Uraniwa Hills and Yokoniwa Rise; Fig. 1b) consisting of peridotitic and gabbroic rocks have been identified within ~15 km of the Kairei [25, 26]. Another, large core complex has been documented on the western slope of the CIR in this area [27]. It was suggested that the combination of the troctolite-alteration at the recharge zone near the oceanic core complex and subsequent basalt-alteration at the discharge zone under the Kairei is causing the distinct chemistry of the hydrothermal fluids [18, 25]. Recent investigations have shown the presence of other hydrothermal deposits (Yokoniwa, and 25°09′S) in the area [26, 28].

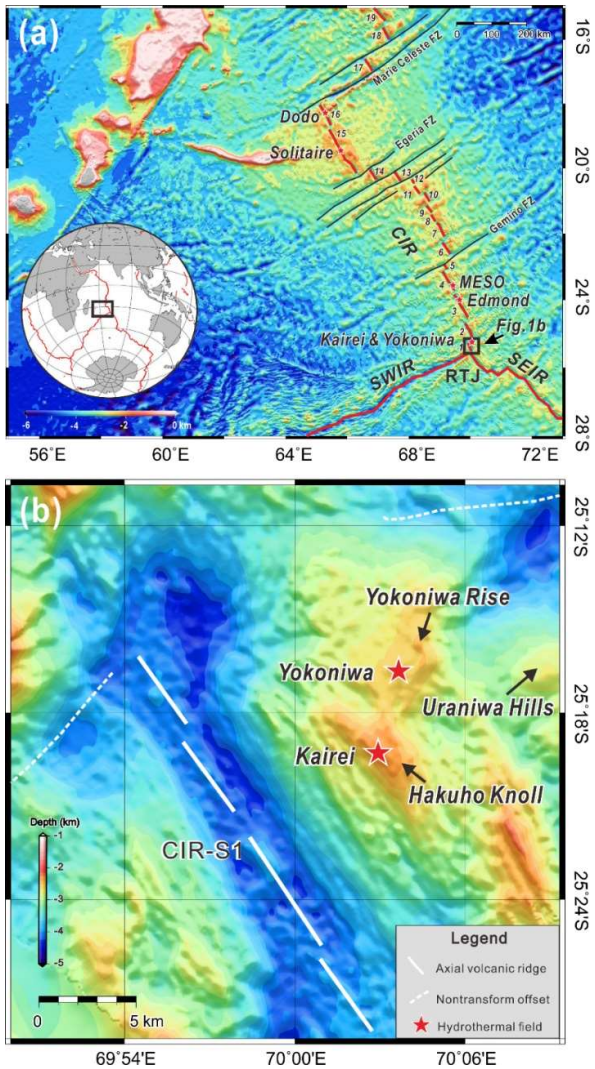

Figure 1

Geological map of the Central Indian Ridge (CIR) and location of the Kairei vent field.

Preprints (www.preprints.org) | NOT PEER-REVIEWED | Posted: 4 September 2018 doi:10.20944/preprints201809.0064.v1

Peer-reviewed version available at Minerals 2018, 8, 526; doi:10.3390/min8110526

Other known hydrothermal fields are indicated by red stars. Note, segment numbering is from Okino et al. (2015) [58]. SWIR = Southwest Indian Ridge; SEIR = Southeast Indian Ridge. Bathymetry data source: Global Multi-Resolution Topography (GMRT) synthesis [59].

The main mineralogical characteristics of Zn-rich chimneys and massive sulfide samples from the Kairei vent field were described in Wang et al. (2012, 2014) [4, 29]. Three mineralization stages were identified at this site: (1) a high-temperature stage consisting largely of chalcopyrite, isocubanite, and pyrite; (2) a medium to low temperature stage characterized by the mineral assemblages of sphalerite and pyrite; and (3) a late stage of waning hydrothermal activity and weathering characterized by secondary Cu-(Fe)-sulfides (bornite, digenite, covellite and idaite), Fe-oxyhydroxides, opal-A, and Cu-chloride (paratacamite and atacamite) related to increasing influence of oxygenated seawater. The observed Cu-(Fe)-sulfide sequence of isocubanite → chalcopyrite→bornite (including bornite–digenite intergrowths)→minerals of the Cu–S system (covellite-idaite solid solutions) exist along a path of increasing oxidation and sulfidation state and is common at Kairei. Age dating ($^{230}Th/^{234}U$) of massive sulfides collected from the Kairei shows ages ranging from 8.4 to 96.3 ka [29] indicating a prolonged hydrothermal history at this site.

3. Samples and methods

The samples from the Kairei are Zn-rich chimneys, Cu-rich massive sulfides, and sulfide-bearing breccias that were recovered using a TV-grab during R/V Dayangyihao DY17A and DY19 cruises in 2005 and 2007 (Table 1). Prior to the laser-ablation analyses, eight polished thin sections were examined microscopically in order to identify the different mineral phases and to avoid measuring grains with visible mineral inclusions. A total of 99 representative analyses was performed by electron microprobe for major element composition [4], and on these samples 64 points were analyzed by Laser Ablation ICP-MS.

Preprints (www.preprints.org) | NOT PEER-REVIEWED | Posted: 4 September 2018 doi:10.20944/preprints201809.0064.v1

Peer-reviewed version available at Minerals 2018, 8, 526; doi:10.3390/min8110526

Table 1
Coordinates of sampling stations and mineral abundances of the sulfides from the Kairei vent field.

Sampling Station	Longitude (E)	Latitude (S)	Depth (m)	Type of Samples	Mineral Assemblage
17A-TVG7-1	70°02.408′	25°19.252′	2430	Cu-rich massive sulfides	cpy+bn+dg+py+(sph+iso+cv+id)
17A-TVG7-3	70°02.408′	25°19.252′	2430	Breccias	q+opal-A+tl+sph+py
17A-TVG9	70°02.420′	25°19.221′	2437	Zn-rich chimney	sph+py+mar+cpy
19III-TVG6	70°02.440′	25°19.230′	2443	Cu-rich massive sulfides	cpy+dg+bn+cv+py+iso+id
19III-TVG7	70°02.410′	25°19.220′	2440	Cu-rich massive sulfides	cpy+dg+bn+cv+py+id

Note: cpy-chalcopyrite, bn-bornite, dg-digenite, py-pyrite, sph-sphalerite, cv-covellite, id-idaite, iso-isocubanite, mar-marcasite, q-quartz, tl-talc

The Laser Ablation ICP-MS study was carried out at GEOMAR, with a 193 nm Excimer laser ablation system (GeoLasPro, Coherent) coupled to a double-focusing, high-resolution magnetic sector mass spectrometer (AttoM, Nu Instruments) in low resolution mode (300 Res, 10% valley definition). Ablation was performed under He carrier gas, additionally Ar carrier gas was mixed in prior to the plasma torch. Spot analysis on sulphides were done by 30 s ablation at a laser repetition rate of 5 Hz, a fluence of 2 J cm^{-2} and a beam diameter of 44 µm. 40 s gas background were collected prior to each ablation. NIST SRM610 (30 s, 10 Hz, 32 µm, 5 J cm^{-2}; [30]) was used for calibration. Additionally a synthetic sulfide standard (trans-1; 30 s, 5 Hz, 44 µm, 2 J cm^{-2}; [31]) was used to calibrate sulfur (39.1 ± 0.1 wt.% S; Wohlgemuth-Ueberwasser pers. comm.). MPI-DING reference glasses (ATHO-G, GOR132-G, KL2-G; 30 s, 10 Hz, 44 µm, 5 J cm^{-2}; [32]) and trans-1 were used as reference materials (results are presented in supplementary table 1). Gas flows, torch position and ion-optics-focusing were optimized in order to provide a maximum in ion transmission, a low polyatomic

Preprints (www.preprints.org) | NOT PEER-REVIEWED | Posted: 4 September 2018 doi:10.20944/preprints201809.0064.v1

Peer-reviewed version available at Minerals 2018, 8, 526; doi:10.3390/min8110526

cluster production rate (ThO/Th ≤ 0.03%; CuAr/Cu < 0.0025%) by hot plasma (normalized argon index NAI≈30; [33]) and a fast sample wash-out. The following isotopes have been monitored: ^{24}Mg, ^{29}Si, ^{51}V, ^{55}Mn, ^{57}Fe, ^{59}Co, ^{60}Ni, ^{63}Cu, ^{66}Zn, ^{71}Ga, ^{73}Ge, ^{75}As, ^{77}Se, ^{95}Mo, ^{107}Ag, ^{111}Cd, ^{115}In, ^{118}Sn, ^{121}Sb, ^{128}Te, ^{135}Ba, ^{197}Au, ^{205}Tl, ^{208}Pb, ^{209}Bi, ^{238}U. Data evaluation has been performed applying the linear regression slope method [34].

4. Results

Full details of the LA-ICP-MS dataset is given in the supplementary table 2, including concentration, analytical precision, and minimum detection limits for each element. The average concentrations of trace elements were calculated for the different minerals and morphologies (Table 2). Representative LA-ICP-MS time-resolved profiles are shown in Figure 2 for pyrite, chalcopyrite, sphalerite, bornite-digenite, and covellite-digenite. Figure 3 shows the trace element distribution in different sulfide mineral phases. In addition, line scan analysis of the pyrite in the Zn-rich chimney sample (17A-TVG9) was carried out and the resulting mass spectrum is shown in Figure 4.

Preprints (www.preprints.org) | NOT PEER-REVIEWED | Posted: 4 September 2018 doi:10.20944/preprints201809.0064.v1

Peer-reviewed version available at Minerals 2018, 8, 526; doi:10.3390/min8110526

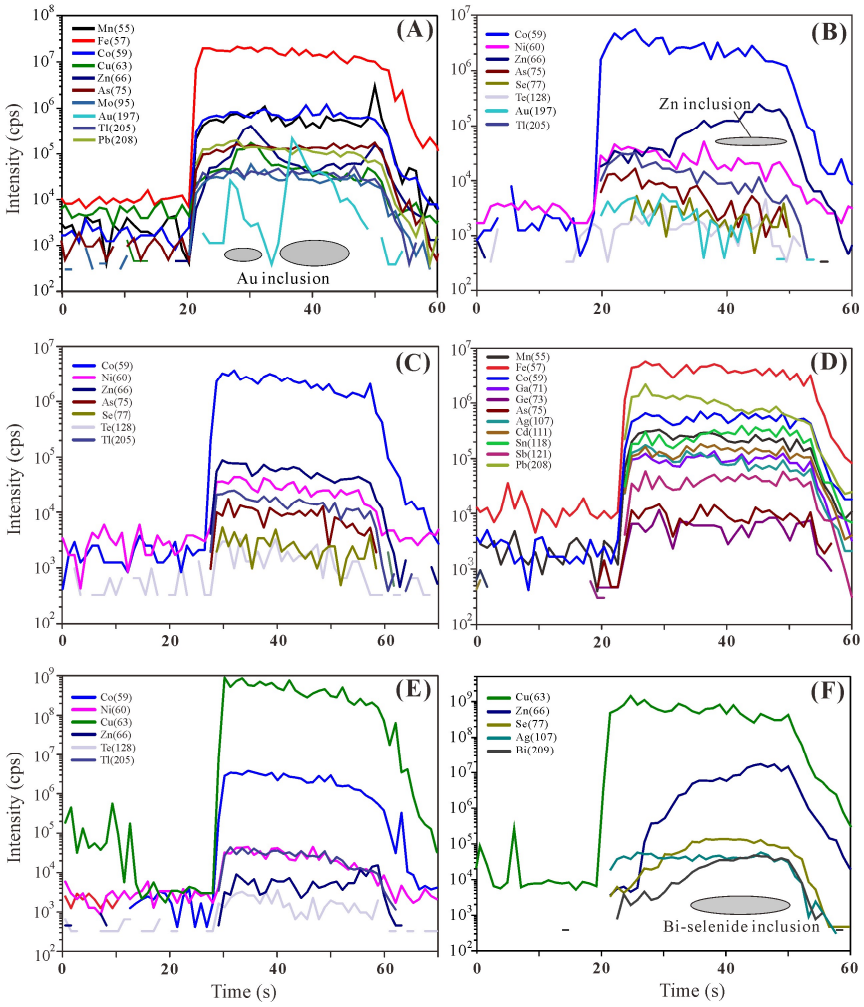

Figure 2

Representative time-resolved LA-ICP-MS depth profiles of selected trace elements in sulfide minerals. (A) subhedral pyrite in the Zn-rich chimney sulfides with Au inclusion; (B) chalcopyrite in the Cu-rich massive sulfide samples with Zn inclusions; (C) chalcopyrite with homogeneous trace elements distribution, shows a homogeneous distribution of Co, As, Mo, and Pb; (D) sphalerite with co-varying of Fe and Co, Ag, Ga, Sn, and Mn; (E) early bornite with homogeneous Co, Ni and Te distribution indicated by the flat concentration patterns; (F) early bornite with Bi-selenide inclusions.

Preprints (www.preprints.org) | NOT PEER-REVIEWED | Posted: 4 September 2018 doi:10.20944/preprints201809.0064.v1

Peer-reviewed version available at Minerals 2018, 8, 526; doi:10.3390/min8110526

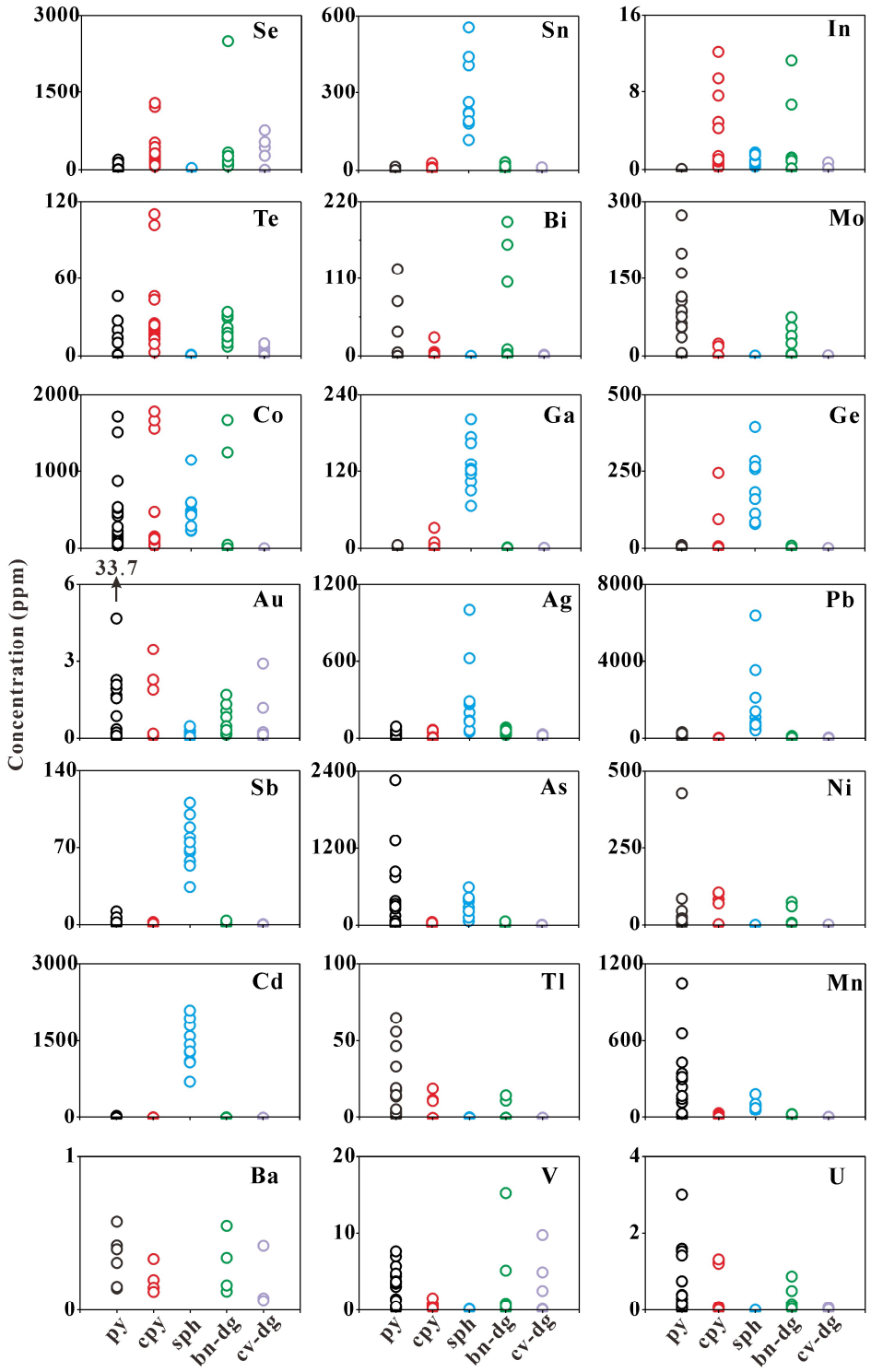

Figure 3
Distribution of trace elements in sulfides from the Kairei vent field. Abbreviations: bn-dg = bornite-digenite intergrowths, cpy = chalcopyrite, cv-dg = covellite-digenite intergrowths, py = pyrite, sph = sphalerite.

Preprints (www.preprints.org) | NOT PEER-REVIEWED | Posted: 4 September 2018 doi:10.20944/preprints201809.0064.v1

Peer-reviewed version available at Minerals 2018, 8, 526; doi:10.3390/min8110526

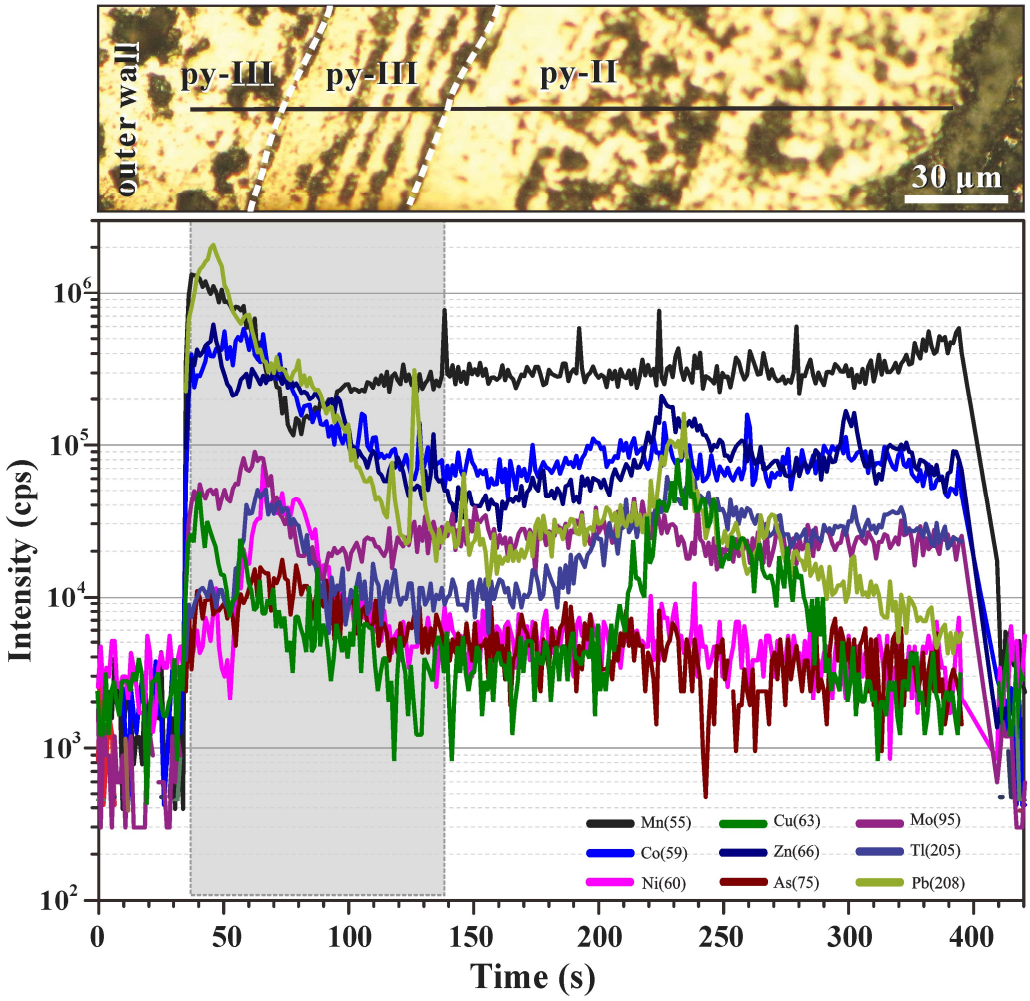

Figure 4

Signal sequence of a line scan analysis of colloform pyrite III and subhedral pyrite II in sample 17A-TVG9. The mass spectrum of colloform pyrite III is marked by high trace element concentrations (Mn, Pb, Cu, Zn, Co, and Mo) that generally decrease towards more homogeneous subhedral pyrite II.

Table 2

Averaged trace element concentrations from LA-ICP-MS for the sulfides of the Kairei vent field.

Mineral	ppm (*n*)	Se	Sn	Te	Bi	Mo	Co	Ga	Ge	Au	Ag	Pb	Sb	As	Ni	Cd	Tl	Mn	U
py all	avg.(*19*)	30.6	1.72	6.35	12.9	69.4	4.20	0.56	2.20	1.16*	2.09	7.32	1.99	35.7	31.1	6.06	1.57	2.40	0.58

Preprints (www.preprints.org) | NOT PEER-REVIEWED | Posted: 4 September 2018 doi:10.20944/preprints201809.0064.v1

Peer-reviewed version available at *Minerals* **2018**, *8*, 526; doi:10.3390/min8110526

py-I	avg.(*8*)	69.57	1.57	14.77	30.66	25.08	44.83	0.53	2.19	1.08	13.30	7.33	0.83	16.30	59.84	46.47	6.43	5.32	0.12
py-II	avg.(*5*)	1.91	0.67	0.42	b.d.l	53.74	27.40	0.72	1.96	0.65*	14.6	0.66	1.66	30.90	2.66	1.59	4.59	7.48	0.84
py-III	avg.(*6*)	2.63	2.79	0.13	0.01	14.22	50.74	0.84	2.42	0.82	36.88	0.82	3.86	60.55	0.58	0.87	4.75	2.85	0.99
cpy	avg.(*16*)	361	10.11	29.57	2.77	4.08	44.85	3.05	22.58	0.50	14.01	4.71	0.26	8.58	23.63	6.02	2.62	1.22	0.25
sph	avg.(*10*)	24.76	28.61	0.21	0.06	0.04	49.12	1.29	20.98	0.13	30.04	176.60	73.36	31.22	0.27	143.33	0.07	92.22	b.d.l
bn-dg	avg.(*10*)	40.03	12.19	19.73	7.35	3.52	30.21	0.51	15.58	0.66	53.63	25.35	0.79	17.79	14.77	3.39	26.49	3.39	0.19
cv-dg	avg.(*9*)	22.23	1.91	2.53	0.25	0.14	0.33	0.30	0.09	0.53	15.55	7.17	0.09	1.23	0.16	1.05	0.02	2.74	0.01

Note: Avg.= average content of trace element; *n*= number of analyses; b.d.l = below the minimum detection limit.

*=excluding outlier in sample 17-9C (see supplementary table 2)

Preprints (www.preprints.org) | NOT PEER-REVIEWED | Posted: 4 September 2018 doi:10.20944/preprints201809.0064.v1

Peer-reviewed version available at Minerals 2018, 8, 526; doi:10.3390/min8110526

4.1. Pyrite

A total of nineteen spot analyses was completed on pyrites selected from different samples of the Kairei vent field, including eight euhedral pyrites (py-I), five subhedral pyrites (py-II), and six colloform pyrites (py-III). Pyrite is generally enriched in Mo, Au, As, Tl, Mn, and U in comparison to the other investigated sulfide minerals (Fig.3, Table 2). Pyrite with different textures shows distinct variations in the trace element contents (Figs.4 and 5, Table 2). Compared to the other textural types, euhedral pyrite I tends to have higher contents of Se (average: 69.5 ppm), Ni (average: 59.8 ppm), Bi (average: 30.6 ppm), and Te (average: 14.7 ppm), when compared to the other textural types. Colloform pyrite III is enriched in Mo (average: 142 ppm), Pb (average: 108 ppm), and U (average: 1.0 ppm) but is poor in Se, Te, Bi, and Au. Subhedral pyrite II is poor in most trace elements, but one single spot shows enhanced Au contents of 33.7 ppm (supplementary table 2). However, enrichments of As (up to 2262 ppm) and Co (up to 1719 ppm) are common in all generations of pyrites. Py-I contains 448 ppm Co and 160 ppm As on average, py-II has As and Co concentrations of 300 ppm and 270 ppm, while py-III are characterized by 665 ppm As and507 ppm Co on average.

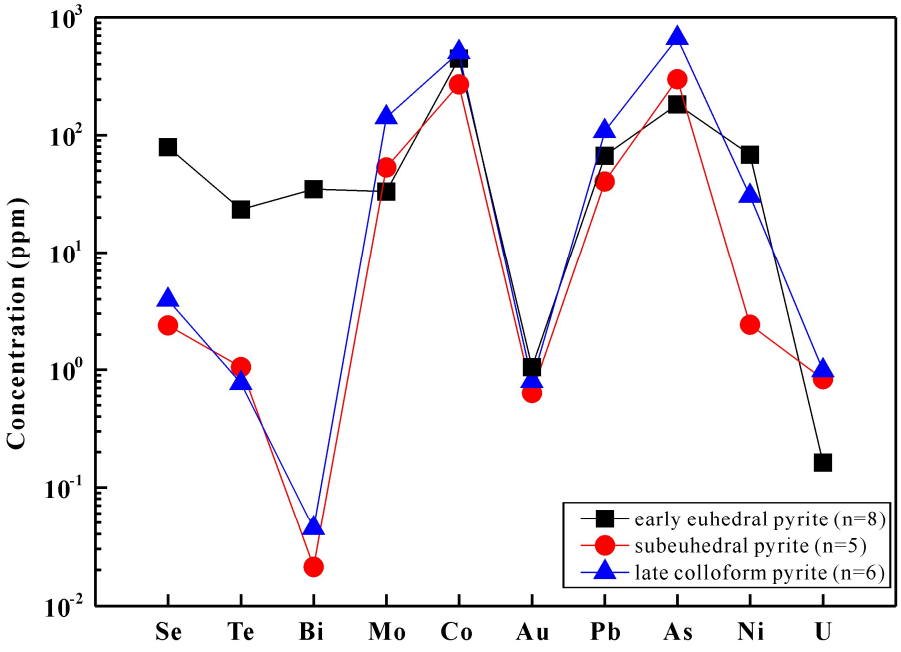

Figure 5

Average trace elements composition in different pyrite types of the Kairei vent field.

Preprints (www.preprints.org) | NOT PEER-REVIEWED | Posted: 4 September 2018 doi:10.20944/preprints201809.0064.v1

Peer-reviewed version available at Minerals 2018, 8, 526; doi:10.3390/min8110526

A line scan analysis in chimney sample 17A-TVG9 was conducted across a boundary between colloform pyrite III and subhedral pyrite II (Fig. 4) exemplifies the differences. Ablation of colloform pyrite III is marked by high trace element concentrations (Mn, Pb, Cu, Zn, Co, and Mo) that generally decrease towards more homogeneous subhedral pyrite II.

4.2. Chalcopyrite

Chalcopyrite (n=16) is characterized by high concentrations of Co (up to 1785 ppm; average: 445 ppm), Se (up to 250 ppm; average: 361 ppm), Te (up to 110 ppm; average: 29.5 ppm). The mean concentrations of Mo, Ag, Pb, Sb, As, Cd, and Mn are generally lower compared to those in the other minerals, however, single measurements with enrichments in Ge (244 ppm) and Au (3.5 ppm) do occur (Fig.3, supplementary table 2).

4.3. Sphalerite

Sphalerite (n=10) from Zn-rich chimneys is characterized by high average concentrations of Pb (1760 ppm), Cd (1433 ppm) Co (491 ppm), As (312 ppm), Ag (304 ppm), Sn (286 ppm), Ge (208 ppm), Ga (129 ppm), and Sb (73.6 ppm). Sphalerite is depleted in Se, Te, Bi, Mo, Au, Ni, Tl, Mn, Ba, V, and U when compared to the other minerals (Fig.3, Table 2).

4.4. Bornite-Digenite assemblage

A total of ten measurements were performed on bornite-digenite intergrowths in the Cu-rich sulfide samples. The results given in Table 2 indicate that bornite-digenite intergrowths are depleted in most trace elements when compared to the other minerals, except for Se , Co and Bi (average: 403, 302 and 47.3 ppm, respectively). Interestingly, the highest concentrations of Se (up to 2504 ppm) and Bi (up to 191 ppm) in all the sulfide minerals were observed in a bornite-digenite grain.

Preprints (www.preprints.org) | NOT PEER-REVIEWED | Posted: 4 September 2018 doi:10.20944/preprints201809.0064.v1

Peer-reviewed version available at Minerals 2018, 8, 526; doi:10.3390/min8110526

4.5. Digenite-Covellite assemblage

Digenite-covellite intergrowths (n=9) from Cu-rich chimneys are characterized by generally low trace element concentrations (Fig.3, Table 2). Exceptions are Se (average: 223 ppm), Ag (average: 15.5 ppm) and 2.9 ppm Au on a single spot.

5. Discussion and Conclusion

5.1. Controls on trace elements in pyrite

Pyrite is the most common sulfide in hydrothermal ores and large mineral chemical data sets exist for SMS deposits in a wide range of geodynamic settings, including mid-ocean ridges, submarine volcanic arcs and related back-arc basins (e.g., [6, 8, 13, 15, 35-37]). Previous studies have shown that most trace elements present in pyrite likely reside in microinclusions of different grains, except for Cu, Co, Ni, Se, and As, which commonly occur in solid solution and result from Fe or S substitution [8, 38].

Colloform pyrite (py-III) in the Zn-rich chimneys is consistently enriched in Pb, Mo, As and U (Fig.5) relative to the other pyrite varieties. Euhedral pyrite (py-I), which is a main constituent in both, the sulfide-bearing breccia and Zn-rich chimneys, has high concentrations of Se, Te, Ni, Bi, and Au, when compared to the colloform pyrite, but is depleted in Mo and U. Enrichments of Co (mean 412 ppm) and As (mean 376 ppm) are common in all generations of pyrites at the Kairei vent field, and a strong positive correlation is observed between Co and As (R^2 =0.95). This could indicate co-incorporation of the two elements resulting from Co^{2+} and As^{2+} substitution for Fe^{2+}. Variations in the concentrations of Se (1.2 ppm – 198 ppm), Te (0.8 ppm – 46.1 ppm), and Bi (<0.02 ppm – 124 ppm) in pyrite are likely governed by the strong temperature gradient [39]. Nickel concentrations (1.3 ppm – 429 ppm) are generally lower than those for Co in pyrite (Co/Ni=3 – 172), indicating that the investigated samples precipitated at a high-temperature conditions. Similar enrichments of Co in pyrite have been described from Mid-Atlantic Ridge 5°S vent field, with average 602 ppm (Table 3), which might be related to a phase of recent magmatic activity [8]. However, beside

Preprints (www.preprints.org) | NOT PEER-REVIEWED | Posted: 4 September 2018 doi:10.20944/preprints201809.0064.v1

Peer-reviewed version available at Minerals 2018, 8, 526; doi:10.3390/min8110526

pyrite, also chalcopyrite and sphalerite at Kairei have higher Co contents compared to minerals from mafic-hosted vent fields (Table 3; see discussion below), which may indicate an ultramafic influence. Since Zn and Co are strongly positively correlated with Pb (Fig. 4), as well as the ratio of Zn/Co has a positive correlation with Pb/Co (Fig. 6), Zn, Co, and Pb may be co-enrichments in the pyrites. Higher contents of Au (33.7 ppm) are most likely related to inclusions of native Au which were observed in a single grain (Fig.2A), similar to observations by Keith et al. (2016) [8]. Uranium, which is normally derived from seawater, is also enriched in colloform pyrite compared to the other pyrite textures. Such U enrichment is commonly observed in the SMS deposits (e.g., [10, 15, 40]).

5.2. Controls on trace elements in chalcopyrite

Chalcopyrite is enriched in Co, Se, and Bi [7] and is the dominated sulfide in SMS deposits, especially in ultramafic environments [3]. Recently, several papers reported LA-ICP-MS-based trace element data of chalcopyrite from basaltic-, ultramafic-, and felsic-hosted SMS deposits worldwide (e.g., [13-15]). Wohlgemuth-Ueberwasser et al. (2015) [13] and documented that the Au, Sb, As, Se, and Te enrichments in chalcopyrite, are mainly controlled by submicroscopic inclusions often as a function of fluid temperature.

Our analyses show that Se (average of 361 ppm) and Te (average of 31.5 ppm) are enriched in chalcopyrite from the Kairei vent field, with a strong positive correlation between these elements (R^2=0.98). Both elements are likely incorporated into the chalcopyrite lattice at high temperatures, with high solubilities of Se and Te in reduced hydrothermal fluids of ~350°C [10, 41-43]. Similar enrichments of Te in chalcopyrite have been described from Logatchev and Semyenov-2, with Te concentrations of 39.6 and 42.0 ppm, respectively (Table 3; [13, 14]). However, the Te content of chalcopyrite in most other SMS deposits is typically low. LA-ICP-MS analyses of chalcopyrite from Wocan, Turtle Pits, and PacManus yielded an average Te concentration around 1 ppm (Table 3; [13, 15]). Compared to the basaltic-hosted Wocan, the Kairei chalcopyrite is

Preprints (www.preprints.org) | NOT PEER-REVIEWED | Posted: 4 September 2018 doi:10.20944/preprints201809.0064.v1

Peer-reviewed version available at Minerals 2018, 8, 526; doi:10.3390/min8110526

also highly enriched in Co with a wide range in concentrations from 32.2 ppm to 1785 ppm (Table 3; [15]), which could be derived from ultramafic rocks in the reaction zone. Maslennikov et al. (2009) [39] suggested the Co enrichment in chalcopyrite from fossil vent chimneys which found in a volcanogenic-hosted massive sulfide deposit in the southern Urals, was related to the Co-bearing minerals inclusions, such as cobaltite, arsenides, sulfoarsenides, and telluride. However, there is no positive correlation observed between the concentrations of Co and Te/As in chalcopyrite from the Kairei vent field the pattern of the Co signal sequence is regular (Fig.2B, C), indicating that Co most likely substitutes Fe. Antimony (<2.3 ppm) and As concentrations (<50.7 ppm) are relatively low in chalcopyrite from Kairei. These concentrations are similar to those reported from other SMS deposits from global mid-ocean ridge systems (Table 3), for example, chalcopyrite from Turtle Pits, Logatchev, Wocan, and Semyenov-2 have a low concentration of Sb (average usually <30 ppm). In contrast, Sb-rich chalcopyrite is common in back-arc basins and the enrichment there is thought to be mainly controlled by the occurrence of Sb-bearing mineral inclusions related to the input of magmatic volatiles [13]. Most chalcopyrite from the Kairei contains < 0.2 ppm Au, however, single measurements with enrichments in Au (3.5 ppm, 2.3 ppm; supplementary table 2) do occur and their spectra indicate the occurrence of native gold inclusions (Fig.2B).

Preprints (www.preprints.org) | NOT PEER-REVIEWED | Posted: 4 September 2018 doi:10.20944/preprints201809.0064.v1

Peer-reviewed version available at Minerals 2018, 8, 526; doi:10.3390/min8110526

Table 3

Average content (ppm) of selected trace elements in the sulfide minerals at the seafloor hydrothermal systems.

Region	Vent Field	Hosted Rock	Minerals	*n*	Co	Ni	As	Se	Sb	Te	Au	Source*
Central Indian Ridge	Kairei	Ultramafic	py	*19*	420	44.4	376	38.7	2.53	15.1	1.16	1
	Kairei	Ultramafic	cpy	*16*	445	53.2	22.9	361	1.03	31.5	1.15	1
	Kairei	Ultramafic	sph	*10*	491	1.37	312	24.7	73.6	0.69	0.16	1
	Kairei	Ultramafic	bn-dg	*10*	302	36.8	25.3	403	1.13	19.9	0.66	1
	Kairei	Ultramafic	cv-dg	*9*	0.59	1.48	3.68	401	0.21	3.80	0.60	1
	Kairei	Ultramafic	py	*39*	279	22.2	179	9.49	1.89		2.31	2
	MESO	Basaltic	py	*77*	392	1.41	909	745	9.21		0.89	2
Carlsberg Ridge	Wocan	Basaltic	py	*19*	110	11.8	224	36.4	3.91	1.40	0.43	3
	Wocan	Basaltic	dg	*11*	0.09	1.51	16.6	0.90	2.96	0.10	0.56	3
	Wocan	Basaltic	bn	*11*	0.11	0.30	0.67	2.54	5.17	0.24	0.36	3
	Wocan	Basaltic	sph	*17*	0.06	0.15	726	0.37	86.0	0.20	0.42	3
	Wocan	Basaltic	cpy	*22*	0.11	0.41	235	52.4	23.0	0.88	0.49	3
Mid-Atlantic Ridge	Logatchev	Ultramafic	py	*34*	102	19.3	47.2	9.56	12.2		1.23	2
	Logatchev	Ultramafic	cc	*15*			42.5	87.9	17.8	4.40	4.92	4
	Logatchev	Ultramafic	cpy	*29*			92.4	119	22.0	39.2	3.12	4
	Logatchev	Ultramafic	cc-cv	*12*			6.75	bdl	1.38	7.30	0.55	4
	Logatchev	Ultramafic	py	*23*			326	15.5	11.2	0.58	4.18	4
	Logatchev	Ultramafic	sph	*10*			214	1.68	233	0.73	3.73	4
	Semeynov-1	Ultramafic	py	*21*	2.07	0.81	510	9.20		0.51	33.1	5
	Semeynov-2	Ultramafic	cpy	*5*	340	13.0	1144	288	25.0	42.0	0.15	6
	Semeynov-2	Ultramafic	sph-wurt	*6*	84.0	0.20	424	129	214	8.51	3.00	6
	Semeynov-2	Ultramafic	cv-A	*8*	21.0	3.00	421	1024	579	97.0	173	6
	Semeynov-2	Ultramafic	cv-B	*3*	9.00	1.00	82.0	222	81.0	48.0	72.0	6

Preprints (www.preprints.org) | NOT PEER-REVIEWED | Posted: 4 September 2018 doi:10.20944/preprints201809.0064.v1

Peer-reviewed version available at Minerals 2018, 8, 526; doi:10.3390/min8110526

	Turtle Pits	Basaltic	cpy	*15*			37.9	204	0.46	4.73	0.06	4
	Turtle Pits	Basaltic	py	*40*			224	25.2	4.94	1.20	0.25	4
	Turtle Pits	Basaltic	sph	*20*			147	28.2	47.9	0.62	0.36	4
	TAG	Basaltic	py	*61*	269	2.28	60.9	43.4	1.55		0.23	2
	5°S	Basaltic	py	*34*	602	1.12	742	30.1	4.57		0.33	2
Valu Fa Ridge	Hine Hina	Basaltic-andesitic	py	*65*	144	16.0	33.2	26.5	1.50		0.61	2
Okinawa Though	Jade	Basaltic-rhyolitic	py	*39*	2.22	2.84	688	44.9	18.0		0.73	2
Kermadec Arc	Brothers	Dacitic	py	*77*	210	2.42	896	481	2.97		0.36	2
Tonga Arc	Volcano 19 (cone)	Basaltic-basaltic andesitic	py	*114*	16.1	1.13	9100	11.0	34.3		12.2	2
	Volcano 19 (caldera)	Basaltic-basaltic andesitic	py	*76*	0.80	3.01	10240		623		1.55	2
Manus Basin	PacManus-RR	Basaltic-rhyolitic	py	*58*			2635	7.39	188	1.10	7.71	4
	PacManus-RR	Basaltic-rhyolitic	cpy	*75*			470	23.5	84.5	0.32	4.84	4
	PacManus-RR	Basaltic-rhyolitic	sph	*52*			1664	3.57	1576	0.02	43.3	4
	PacManus-SM	Basaltic-rhyolitic	cc	*5*			749		304	0.69	4.16	4
	PacManus-SM	Basaltic-rhyolitic	cpy	*25*			15237	1.39	875	1.66	4.99	4
	PacManus-SM	Basaltic-rhyolitic	py	*5*			5390	5.97	29.4		8.16	4
	PacManus-SM	Basaltic-rhyolitic	sph	*6*			17269	9.42	167		2.45	4
		MORB			56	200	0.11	0.21	14×10^{-3}	4.9×10^{-3}	1.2×10^{-3}	7

*Note:

1-this study; 2-Keith et al. (2016) [8]; 3-Wang et al. (2017) [15]; 4-Wohlgemuth-Ueberwasser et al. (2015) [13]; 5-Melekestseva et al. (2014) [54]; 6-Melekestseva et al. (2017) [48]; 7-Arevalo and McDonough (2010) [55] and reference therein.

Preprints (www.preprints.org) | NOT PEER-REVIEWED | Posted: 4 September 2018 doi:10.20944/preprints201809.0064.v1

Peer-reviewed version available at *Minerals* **2018**, *8*, 526; doi:10.3390/min8110526

5.3. Controls on trace elements in sphalerite

As one of the major sulfide minerals in the SMS deposits, sphalerite precipitates under a range of temperature, pressure, sulfur and oxygen fugacity conditions [44]. At Kairei, sphalerite from the Zn-rich chimney is highly enriched in Cd, Pb, Co, As, Sn, Ga, Ge, Ag, and Sb compared to the other minerals. Cadmium, Co, Ga, and Sn show a clear positive correlation with increasing temperature (Fig. 7) calculated following the $Fe/Zn_{sphalerite}$ equation of Keith et al. (2014) [45]. In contrast, Ag, As, Ge, and Pb are characterized by negative correlations with temperature and precipitate as a consequence of increasing fO_2 of the hydrothermal fluids due to significant mixing with seawater (Fig. 7). Trace element concentrations in sphalerite show strong positive correlations (Fig. 8) for Pb-Ag (R^2=0.98), Pb-Au (R^2=0.98), Co-Fe (R^2=0.98), Co-Cd (R^2=0.73), Cu-Sn (R^2=0.80), Ga-Sn (R^2=0.92), As-Ge (R^2=0.95), and Sb-Cd (R^2=0.88). The high concentration of Cd (703 ppm – 2100 ppm) and Co (226 ppm– 1150 ppm) are likely caused by the substitution of Zn^{2+} by Cd^{2+} and Co^{2+} (e.g., [44, 46]). A high concentration of Pb (hundreds to thousands of ppm) accompanied by high Ag concentration (52 ppm– 1005 ppm) in sphalerite, most likely indicates that the Ag occurs in microinclusions of galena. The concentration of Au is generally low in sphalerite (<0.5 ppm), however, it is related to Pb (R^2_{Ag-Au}=0.69), suggesting co-precipitation with Au as electrum inclusions in galena. The positive correlation between Sn and Cu as well as for Sn and Ga, may be attributed to the substitution of Zn^{2+} by Ga^{2+} or Ga^{3+} [12], or $3Zn^{2+}$ by Sn^{4+} + Cu^{2+} [44]. This substitution would furthermore explain the Sn enrichment in bulk samples from Zn-rich chimneys (up to 245 ppm; [4]). Sphalerite is also enriched in Ge and As, with concentrations ranging from 79 ppm to 396 ppm and 66 ppm to 592 ppm, respectively, similar to sphalerite from the Wocan hydrothermal field at the Carlsberg Ridge [15]. Although Ge^{4+} represents the more common oxidation state, Cook et al. (2009) [44] proposed a direct $Ge^{2+} \leftrightarrow Zn^{2+}$ substitution in sphalerite. The strong correlation of As with Ge (R^2=0.95) in sphalerite from Kairei suggests that they might precipitate under medium-

Preprints (www.preprints.org) | NOT PEER-REVIEWED | Posted: 4 September 2018 doi:10.20944/preprints201809.0064.v1

Peer-reviewed version available at Minerals 2018, 8, 526; doi:10.3390/min8110526

temperature and moderately reduced conditions [44].

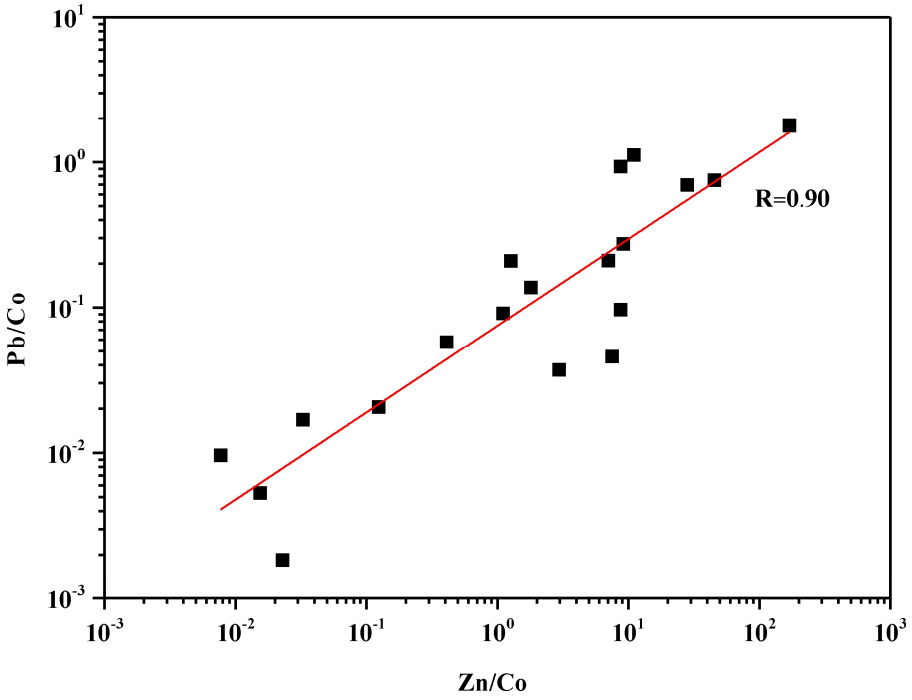

Figure 6

Variations of Zn/Co vs. Pb/Co in pyrite from the Kairei vent field.

Preprints (www.preprints.org) | NOT PEER-REVIEWED | Posted: 4 September 2018 doi:10.20944/preprints201809.0064.v1

Peer-reviewed version available at Minerals 2018, 8, 526; doi:10.3390/min8110526

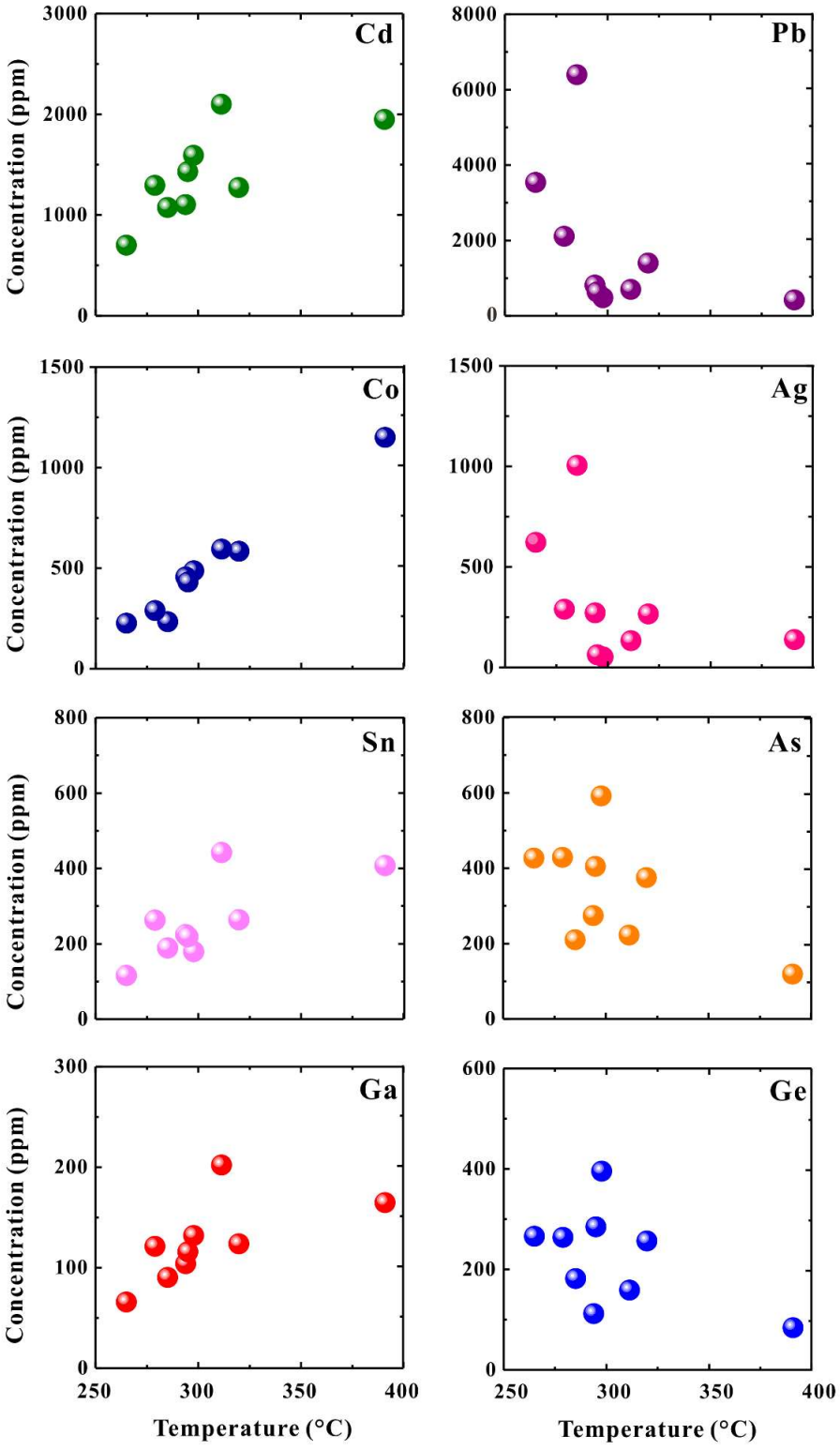

Figure 7

Correlation between the concentration of trace elements in sphalerite and precipitation temperatures calculated from Keith et al. (2016) [8].

Preprints (www.preprints.org) | NOT PEER-REVIEWED | Posted: 4 September 2018 doi:10.20944/preprints201809.0064.v1

Peer-reviewed version available at Minerals 2018, 8, 526; doi:10.3390/min8110526

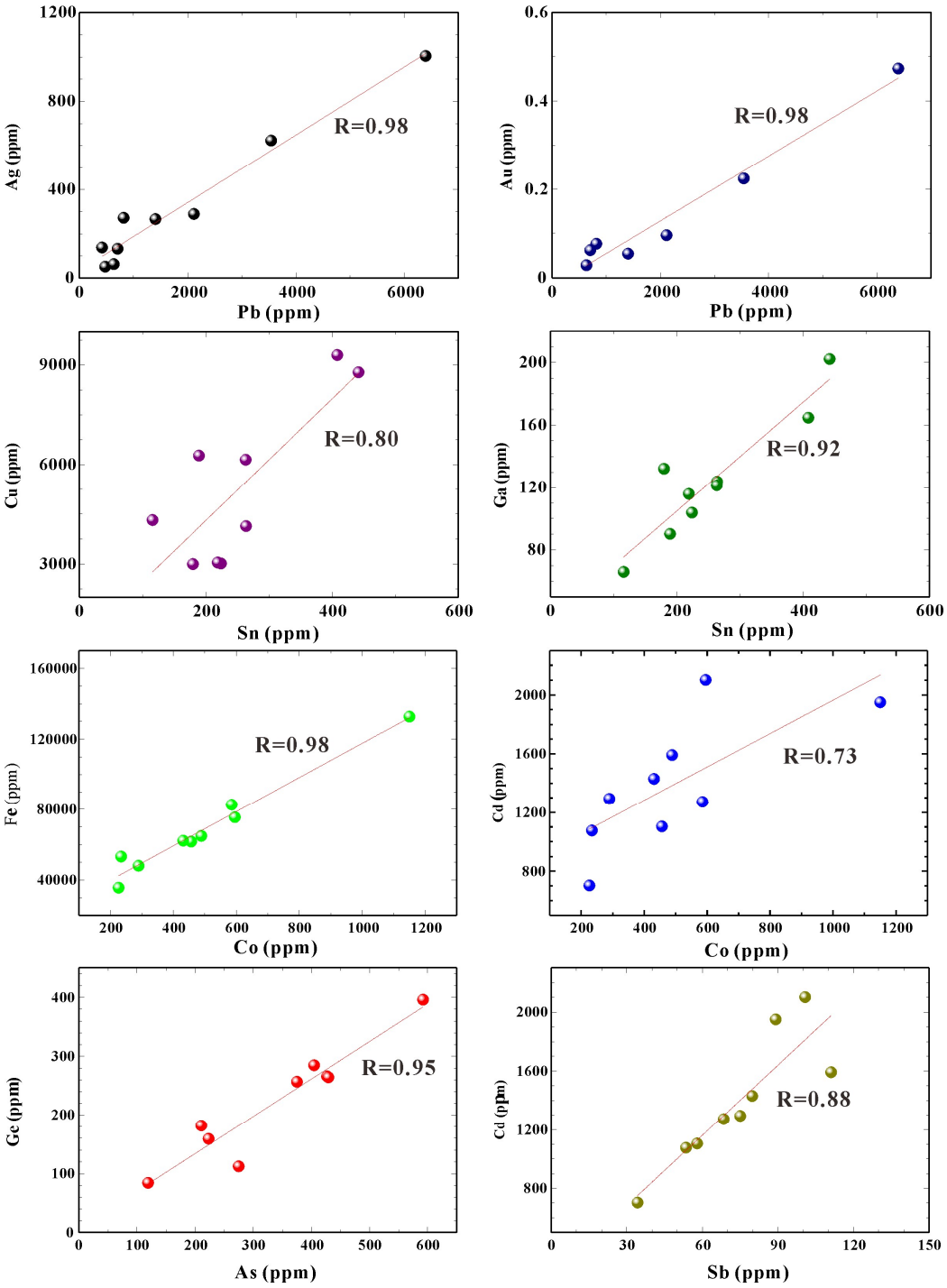

Figure 8

Trace element correlations of sphalerite for Pb-Ag, Pb-Au, Sn-Cu, Sn-Ga, Co-Fe, Co-Cd, As-Ge, and Sb-Cd from Zn-rich chimney samples.

Preprints (www.preprints.org) | NOT PEER-REVIEWED | Posted: 4 September 2018 doi:10.20944/preprints201809.0064.v1

Peer-reviewed version available at Minerals 2018, 8, 526; doi:10.3390/min8110526

5.4. Controls on trace elements in bornite, digenite and covellite

Bornite, digenite, and covellite are common Cu-(Fe)-sulfide minerals in SMS deposits, which often precipitate under more oxidizing conditions caused by ingress of seawater during the waning stages of hydrothermal activity (e.g., [3, 4, 43, 47]). Due to the interaction of hydrothermal fluids with cold, oxygenated seawater, U, V, and sometimes Ag may reach high concentrations in low-T bornite and digenite forming during the latest phase or during oxidation of primary sulfides (e.g., [14, 15, 48]). In contrast, bornite precipitated at higher temperatures is shown to have relatively high concentrations of Sn and In [15]. Additionally, Cook et al. (2011) [49] addressed that high-T primary bornite is an excellent host for Bi and Se. In our dataset the higher Bi (up to 191 ppm) and Se (up to 2500 ppm) concentrations are found in bornite, and may be explained by abundant Bi-selenide inclusions (Fig.2F). Cobalt concentrations in bornite and digenite are typically close to their respective minimum detection limits. However, in some spots high Co concentrations (>1000 ppm; Fig.3) are observed, and based on the regular pattern of the Co signal sequence, we suppose this as local substitution of Co into the Fe site within bornite (Fig.2E).

5.5. Comparison with mafic- and ultramafic-hosted SMS deposits

The concentrations of trace elements in the ores from the SMSs, especially those that are mobilized at relatively low temperatures, are remarkably sensitive to the source rock concentrations in different tectonic setting (e.g., [3, 7, 50]). For example, mafic- and ultramafic-hosted SMSs at mid-ocean ridges are commonly enriched in Co and Ni [3, 4, 51], whereas the felsic-hosted deposits related to the volcanic arc settings are enriched in Pb, As, Sb, Ag, and Sn [7]. Previous studies concluded that the presence of elevated Ni and Co in the sulfides from ultramafic SMS deposits is thought derived from the ultramafic substrate (1960 ppm Ni and 106 ppm Co in depleted mantle versus 104 ppm Ni and 44 ppm Co in MORB [52, 53]). However, the depositional conditions may also play a significant role in determining the final metal concentrations in the sulfide minerals [51].

Preprints (www.preprints.org) | NOT PEER-REVIEWED | Posted: 4 September 2018 doi:10.20944/preprints201809.0064.v1

Peer-reviewed version available at Minerals 2018, 8, 526; doi:10.3390/min8110526

Pyrite from the ultramafic-hosted Kairei, Logatchev and Semyenov-1 has higher concentrations of Au (> 1 ppm on average) than those from the mafic-hosted Wocan, MESO, TAG, Turtle Pits and MAR 5°S (Au <1 ppm) along the mid-ocean ridge (Table 3; Fig. 9). Keith et al. (2016) [8] proposed that serpentinization in ultramafic-hosted hydrothermal systems plays an important role on Au enrichment in pyrite with low As contents. However, compared with felsic-hosted SMS deposits, sulfide minerals from the ultramafic-hosted deposits show higher concentrations of Se and Te, but lower As, Sb, and Au concentrations (Table 3), which is most likely attributed to more reducing conditions at mid-ocean ridges and the contribution of magmatic volatiles in arc-related occurrences [13]. Significant variations of Ni/As versus Au/As ratios in pyrite are observed between ultramafic- and mafic-hosted SMS occurrences (Fig. 9). This implies that an ultramafic influence on Au and Ni enrichment in pyrite from Kairei is detectable. However, the ultramafic-hosted Semyenov-1 show lower Ni with higher Au (33.1 ppm in average) and As (510 ppm) concentrations (Table 3; Fig. 9), Melekestseva et al. (2014) [54] suggested that a mafic substrate might make contribution to those elements in the Semyenov-1. Clearly, investigations on the trace element behavior in other ultramafic-hosted sites such as Rainbow, Ashadze and others are needed to verify this observation.

In order to be able to compare the differences in trace element concentrations of chalcopyrite between ultramafic/mafic- and felsic-hosted deposits we normalized the trace elements to global MORB [55] (Fig.10). Chalcopyrite from Kairei shows higher concentration of Se relative to Wocan, Semyenov-2, and Logatchev, but lower concentrations in As and Sb (Table 3; Fig. 10). The general enrichment of Se in chalcopyrite is a factor of fluid temperature, with high solubility of Se in fluids of ~350°C [10, 41, 56]. A host rock influence (mafic versus ultramafic) can probably be neglected since significant Se enrichment in chalcopyrite has been found in both, ultramafic- and mafic-hosted SMSs (e.g., average: ~2000 ppm, Broken Spur [57]).

Preprints (www.preprints.org) | NOT PEER-REVIEWED | Posted: 4 September 2018 doi:10.20944/preprints201809.0064.v1

Peer-reviewed version available at Minerals 2018, 8, 526; doi:10.3390/min8110526

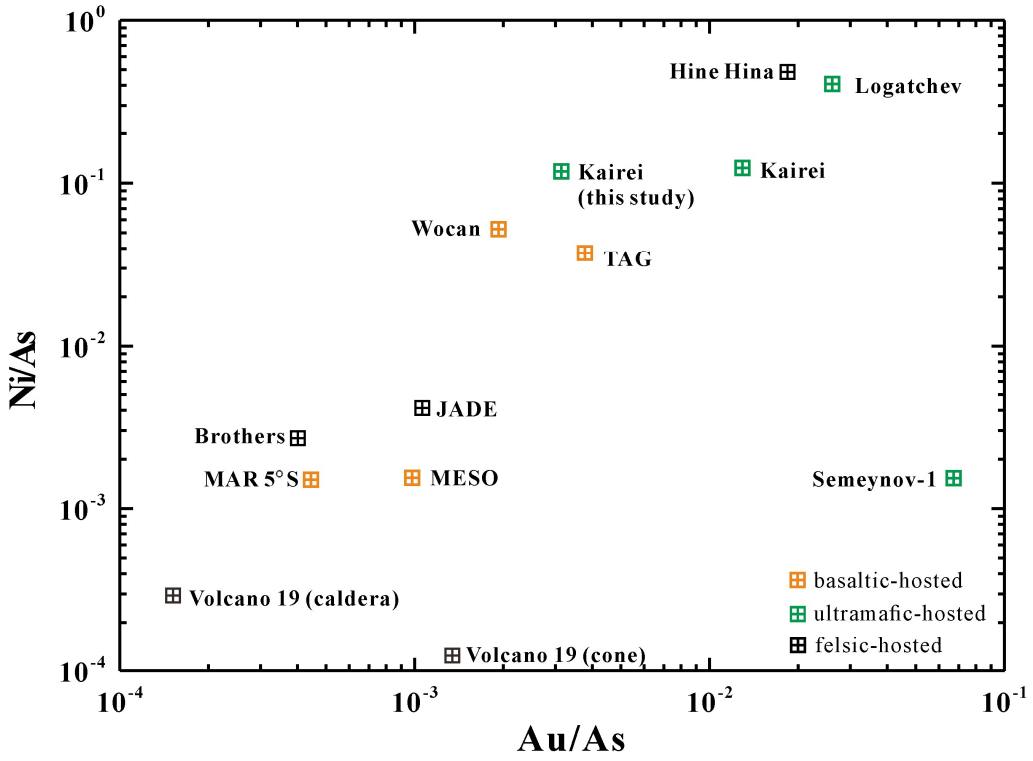

Figure 9

Variations of Ni/As vs. Au/As in pyrite from ultramafic- and mafic-hosted hydrothermal systems at mid-ocean ridges and felsic-hosted sites occurred in the back-arc basin/arc volcanoes. See the data source in Table 3.

Preprints (www.preprints.org) | NOT PEER-REVIEWED | Posted: 4 September 2018 doi:10.20944/preprints201809.0064.v1

Peer-reviewed version available at Minerals 2018, 8, 526; doi:10.3390/min8110526

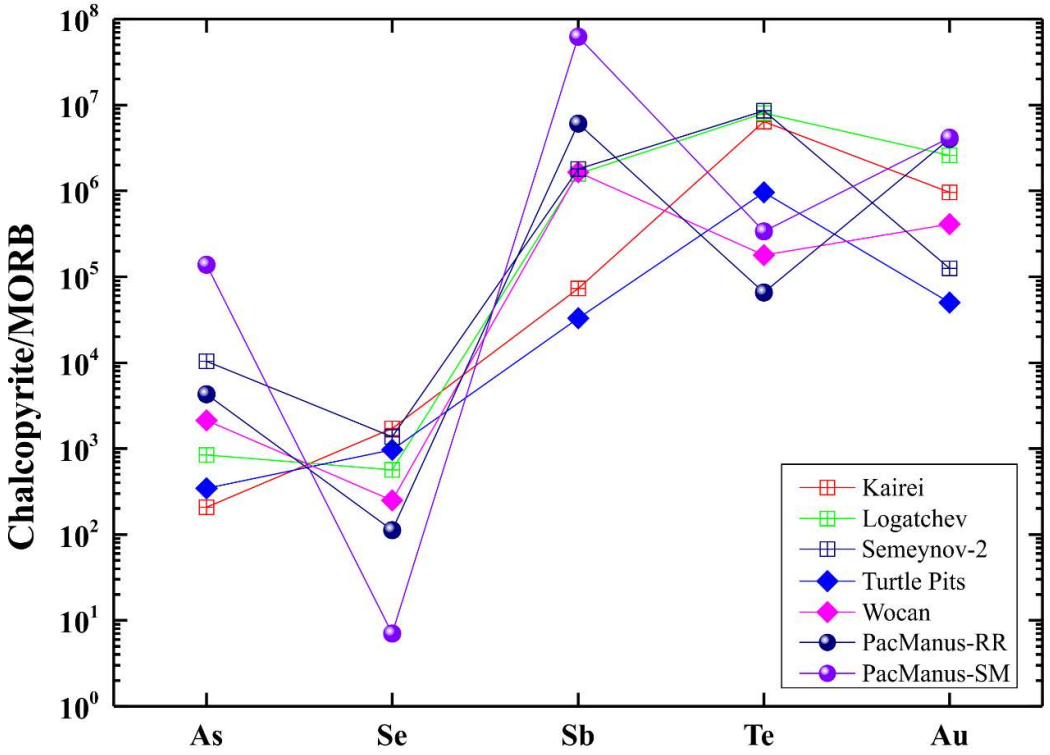

Figure 10

Selected MORB-normalized trace element patterns for chalcopyrite from different seafloor hydrothermal systems. MORB data source from Arevalo and McDonough (2010) [55].

Preprints (www.preprints.org) | NOT PEER-REVIEWED | Posted: 4 September 2018 doi:10.20944/preprints201809.0064.v1

Peer-reviewed version available at Minerals 2018, 8, 526; doi:10.3390/min8110526

Acknowledgements

This study is funded by National Key Research and Development Program of China (2018YFC0309903), China Ocean Mineral Resources R&D Association project (DY135-S2-1-05), the Scientific Research Fund of the Second Institute of Oceanography, SOA (grant number QNYC1701) and Sino-German Cooperation Project on Marine and Polar Research (BMBF grant number 03F0724A). We appreciate the great help from Dagmar Rau for her assistance with the LA-ICP-MS analyses.

References

1. Hannington, M.D.; de Ronde, C.D.; Petersen, S. Sea-floor tectonics and submarine hydrothermal systems. *Eco. Geol.* **2005**, 100th Anniversary Volume, 111-141.
2. Binns, R.A.; Scott, S.D. Actively forming polymetallic sulfide deposits associated with felsic volcanic rocks in the eastern Manus back-arc basin, Papua New Guinea. *Econ. Geol.* **1993**, 88(8), 2226-2236.
3. Fouquet, Y.; Pierre, C.; Etoubleau, J.; Charlou, J.L.; Ondréas, H.; Barriga, F.J.A.S.; Cherkashov, G.; Semkova, T.; Poroshina, I.; Bohn, M.; Donval, J.P.; Henry, K.; Murphy, P.J.; Rouxel, O. Geodiversity of hydrothermal along the Mid-Atlantic Ridge and ultramafic-hosted mineralization: A new type of oceanic Cu-Zn-Co-Au Volcanogenic Massive Sulfide Deposit. In *Diversity of Hydrothermal Systems on Slow Spreading Ocean Ridges*; Rona, P.A., Devey, C.W., Dyment, J., Murton, B.J. Eds.; AGU: Washington, D.C., 2010. pp. 321-367.
4. Wang, Y.; Han, X.; Petersen, S.; Jin, X.; Qiu, Z.; Zhu, J. Mineralogy and geochemistry of hydrothermal precipitates from Kairei hydrothermal field, Central Indian Ridge. *Mar. Geol*. **2014**, 354, 69-80.
5. German, C.R.; Petersen, S.; Hannington, M.D. Hydrothermal exploration of mid-ocean ridges: Where might the largest sulfide deposits be forming? *Chem. Geol*. **2016**, 420: 114-126.
6. Monecke, T.; Petersen, S.; Hannington, M.D.; Grant, H.; Samson, I. The minor element endowment of modern sea-floor massive sulfides and comparison with deposits hosted in ancient volcanic successions. *Reviews in Economic Geology*. **2016**, 18, 245-306.
7. Hannington, M.D. Volcanogenic Massive Sulfide Deposits. In *Treatise on Geochemistry*, 2nd Ed.; Holland, H.D., Turekian, K.K, Eds.; Elsevier: Oxford, 2014. pp. 463-488.
8. Keith, M.; Häckel, F.; Haase, K.M.; Schwarz-Schampera, U.; Klemd, R. Trace element systematics of pyrite from submarine hydrothermal vents. *Ore Geol. Rev.* **2016**, 72, 728-745.

Preprints (www.preprints.org) | NOT PEER-REVIEWED | Posted: 4 September 2018 doi:10.20944/preprints201809.0064.v1

Peer-reviewed version available at Minerals 2018, 8, 526; doi:10.3390/min8110526

9. Fontboté, L.; Kouzmanov, K.; Chiaradia, M.; Pokrovski, G.S. Sulfide Minerals in Hydrothermal Deposits. *Elements*. **2017**, 13(2), 97-103.
10. Butler, I.B.; Nesbitt, R.W. Trace element distributions in the chalcopyrite wall of a black smoker chimney: insights from laser ablation inductively coupled plasma mass spectrometry (LA-ICP-MS). *Earth Planet. Sci. Lett.* **1999**, 167, 335-345.
11. Lein, A.; Bogdanov, Y.; Maslennikov, V.; Li, S.; Ulyanova, N.; Maslennikova, S.; Ulyanov, A. Sulfide minerals in the Menez Gwen nonmetallic hydrothermal field (Mid-Atlantic Ridge). *Lithol. Miner. Resour.* **2010**, 45, 305-323.
12. Ye, L.; Cook, N.J.; Ciobanu, C.L.; Yuping, L.; Qian, Z.; Tiegeng, L.; Wei, G.; Yulong, Y.; Danyushevsky, L.V. Trace and minor elements in sphalerite from base metal deposits in South China: A LA-ICPMS study. *Ore Geol. Rev.* **2011**, 39, 188-217.
13. Wohlgemuth-Ueberwasser, C.C.; Viljoen, F.; Petersen, S.; Vorster, C. Distribution and solubility limits of trace elements in hydrothermal black smoker sulfides: An in-situ LA-ICP-MS study. *Geochim. Cosmochim. Acta.* **2015**, 159, 16-41.
14. Melekestseva, I.Y.; Maslennikov, V.V.; Tret'Yakov, G.A.; Nimis, P.; Beltenev, V.E.; Rozhdestvenskaya, I.I.; Maslennikova, S.P.; Belogub, E.V.; Danyushevsky, L.V.; Large, R.R.; Yuminov, A.M.; Sadykov, S.A. Gold- and Silver-Rich Massive Sulfides from the Semenov-2 Hydrothermal Field, 13°31.13′N, Mid-Atlantic Ridge: A Case of Magmatic Contribution? *Econ. Geol.* **2017a**, 112(4), 741-773.
15. Wang, Y.; Han, X.; Petersen, S.; Frische, M.; Qiu, Z.; Li, H.; Li, H.; Wu, Z.; Cui, R. Mineralogy and trace element geochemistry of sulfide minerals from the Wocan Hydrothermal Field on the slow-spreading Carlsberg Ridge, Indian Ocean. *Ore Geol. Rev.* **2017**, 84,1-19.
16. Gamo, T.; Chiba, H.; Yamanaka, T.; Okudaira, T.; Hashimoto, J.; Tsuchida, S.; Ishibashi, J.; Kataoka, S.; Tsunogai, U.; Okamura, K.; Sano, Y.; Shinjo, R. Chemical characteristics of newly discovered black smoker fluids and associated hydrothermal plumes at the Rodriguez Triple Junction, Central Indian Ridge. *Earth Planet. Sci. Lett.* **2001**, 193, 371-379.
17. Van Dover, C.L.; Humphris, S.E.; Fornari, D.; Cavanaugh, C.M.; Collier, R.; Goffredi, S.K.; Hashimoto, J.; Lilley, M.D.; Reysenbach, A.L.; Shank, T.M.; Von Damm, K.L.; Banta, A.; Gallant, R.M.; Gotz, D.; Green, D.; Hall, J.; Harmer, T.L.; Hurtado, L.A.; Johnson, P.; McKiness, Z.P.; Meredith, C.; Olson, E.; Pan, I.L.; Turnipseed, M.; Won, Y.; Young, C.R.I.; Vrijenhoek, R.C. Biogeography and ecological setting of Indian Ocean hydrothermal vents. *Science* **2001**, 294, 818-823.
18. Kumagai, H.; Nakamura, K.; Toki, T.; Morishita, T.; Okino, K.; Ishibashi, J.; Tsunogai, U.; Kawaguacci, S.; Gamo, T.; Shibuya, T.; Sawaguchi, T.; Neo, N.; Joshima, M.; Sato, T.; Takai, K. Geological background of the Kairei and Edmond hydrothermal fields along the Central Indian Ridge: Implications of their vent fluids' distinct chemistry. *Geofluids*. **2008**, 8(4), 239-251.
19. Gallant, R.M.; Von Damm, K.L. Geochemical controls on hydrothermal fluids from the Kairei

Preprints (www.preprints.org) | NOT PEER-REVIEWED | Posted: 4 September 2018 doi:10.20944/preprints201809.0064.v1

Peer-reviewed version available at Minerals 2018, 8, 526; doi:10.3390/min8110526

and Edmond Vent Fields, 23°–25°S, Central Indian Ridge. *Geochem. Geophys. Geosyst*. **2006**, 7, Q6018.

20. Kelley, D.S.; Karson, J.A.; Blackman, D.K.; Fruh-Green, G.L.; Butterfield, D.A.; Lilley, M.D.; Olson, E.J.; Schrenk, M.O.; Roe, K.K.; Lebon, G.T.; Rivizzigno, P.; the AT3-60 Shipboard Party An off-axis hydrothermal vent field near the Mid-Atlantic Ridge at 30°N. *Nature.* **2001**, 412(6843), 145-149.
21. Douville, E.; Charlou, J L.; Oelkers, E H.; Bienvenu, P.; Jove Colon, C F.; Donval, J P.; Fouquet, Y.; Prieur, D.; Appriou, P. The rainbow vent fluids (36°14′N, MAR): the influence of ultramafic rocks and phase separation on trace metal content in Mid-Atlantic Ridge hydrothermal fluids. *Chem. Geol.* **2002**, 184(1-2), 37-48.
22. Charlou, J.L.; Donval, J.P.; Fouquet, Y.; Jean-Baptiste, P.; Holm, N. Geochemistry of high H_2 and CH_4 vent fluids issuing from ultramafic rocks at the Rainbow hydrothermal field (36°14′N, MAR). *Chem. Geol.* **2002**, 191(4), 345-359.
23. Charlou, J.L.; Donval, J.P.; Konn, C.; Ondréas, H.; Fouquet, Y. High production and fluxes of H_2 and CH_4 and evidence of abiotic hydrocarbon synthesis by serpentinization in ultramafic-hosted hydrothermal systems on the Mid-Atlantic Ridge. In *Diversity of Hydrothermal Systems on Slow Spreading Ocean Ridges*; Rona, P.A., Devey, C.W., Dyment, J., Murton, B.J. Eds., AGU: Washington, D.C., 2010, pp. 265-296.
24. Melchert, B.; Devey, C.W.; German, C.R.; Lackschewitz, K.S.; Seifert, R.; Walter, M.; Mertens, C.; Yoerger, D.R.; Baker, E.T.; Paulick, H.; Nakamura, K. First evidence for high-temperature off-axis venting of deep crustal/mantle heat: The Nibelungen hydrothermal field, southern Mid-Atlantic Ridge. *Earth Planet. Sci. Lett.* **2008**, 275(1-2), 61-69.
25. Nakamura, K.; Morishita, T.; Bach, W.; Klein, F.; Hara, K.; Okino, K.; Takai, K.; Kumagai, H. Serpentinized troctolites exposed near the Kairei Hydrothermal Field, Central Indian Ridge: Insights into the origin of the Kairei hydrothermal fluid supporting a unique microbial ecosystem. *Earth Planet. Sci. Lett.* **2009**, 280(1-4): 128-136.
26. Fujii, M.; Okino, K.; Sato, T.; Sato, H.; Nakamura, K. Origin of magnetic highs at ultramafic hosted hydrothermal systems: Insights from the Yokoniwa site of Central Indian Ridge. *Earth Planet. Sci. Lett.* **2016**, 441, 26-37.
27. Morishita, T.; Hara, K.; Nakamura, K.; Sawaguchi, T.; Tamura, A.; Arai, S.; Okino, K.; Takai, K.; Kumagai, H.; Igneous, alteration and exhumation processes recorded in abyssal peridotites and related fault rocks from an oceanic core complex along the Central Indian Ridge. *Journal of Petrology.* **2009**, 50(7), 1299-1325.
28. Zeng, Z.; Ma, Y.; Chen, S.; Selby, D.; Wang, X.; Yin, X. Sulfur and lead isotopic compositions of massive sulfides from deep-sea hydrothermal systems: Implications for ore genesis and fluid circulation. *Ore Geol. Rev.* **2017**, 87, 155-171.
29. Wang, Y.; Han, X.; Jin, X.; Qiu, Z.; Ma, Z.; Yang, H. Hydrothermal activity events at Kairei Field, Central Indian Ridge 25°S. *Resour. Geol.* **2012**, 62, 208-214.

Preprints (www.preprints.org) | NOT PEER-REVIEWED | Posted: 4 September 2018 doi:10.20944/preprints201809.0064.v1

Peer-reviewed version available at Minerals 2018, 8, 526; doi:10.3390/min8110526

30. Wise, S.; Watters, R. Certificate of analysis, standard reference material 610. *National Institute of Standards and Technology*, http://www.nist.gov/srm. 2012.
31. Wohlgemuth-Ueberwasser, C.C.; McClung, C.R.; Viljoen, F. Metamorphic alteration of the massive sulfide horizon from the Salt River VMS deposit (South Africa). *Ore Geol. Rev*. **2014**, 56, 45–52.
32. Jochum, K.P.; Stoll, B.; Herwig, K.; Willbold, M.; Hofmann, A.W.; Amini, M.; Aarburg, S.; Abouchami, W.; Hellebrand, E.; Mocek, B.; Raczek, I.; Stracke, A.; Alard, O.; Bouman, C.; Becker, S.; Dücking, M.; Brätz, H.; Klemd, R.; de Bruin, D.; Canil, D.; Cornell, D.; de Hoog, C.; Dalpé, C.; Danyushevsky, L.V.; Eisenhauer, A.; Gao, Y.; Snow, J.E.; Groschopf, N.; Günther, D.; Latkoczy, C.; Guillong, M.; Hauri, E.H.; Höfer, H.E.; Lahaye, Y.; Horz, K.; Jacob, D.E.; Kasemann, S.A.; Kent, A.J.R.; Ludwig,T.; Zack, T.; Mason, P.R.D.; Meixner, A.; Rosner, M.; Misawa, K.; Nash, B.P.; Pfänder, J.; Premo, W.R.; Sun, W.; Tiepolo, M.; Vannucci, R.; Vennemann, T.; Wayne, D.; Woodhead, J.D. MPI-DING reference glasses for in situ microanalysis: New reference values for element concentrations and isotope ratios. *Geochem. Geophys. Geosyst.* **2006**, 7, Q02008.
33. Fietzke, J.; Frische, M. Experimental evaluation of elemental behavior during LA-ICP-MS: influences of plasma conditions and limits of plasma robustness. *J. Anal. At. Spectrom.* **2016**, 31, 234-244.
34. Fietzke, J.; Liebetrau, V.; Guenther, D.; Guers, K.; Hametner, K.; Zumholz, K.; Hansteen, T.H.; Eisenhauer, A. An alternative data acquisition and evaluation strategy for improved isotope ratio precision using LA-MC-ICP-MS applied to stable and radiogenic strontium isotopes in carbonates. *J. Anal. At. Spectrom*. **2008**, 23, 955-961.
35. Tivey, M.K.; Humphris, S.E.; Thompson, G.; Hannington, M.D.; Rona, P.A. Deducing patterns of fluid flow and mixing within the TAG active hydrothermal mound using mineralogical and geochemical data. *J. Geophys. Res.* **1995**, 100, 12527-12555.
36. Herzig, P.M.; Hannington, M.D.; Arribas, Jr. A. Sulfur isotopic composition of hydrothermal precipitates from the Lau back-arc: implications for magmatic contributions to seafloor hydrothermal systems. *Miner. Deposita*. **1998**, 33(3), 226-237.
37. de Ronde, C.; Massoth, G.; Butterfield, D.; Christenson, B.; Ishibashi, J.; Ditchburn, R.; Hannington, M.; Brathwaite, R.; Lupton, J.; Kamenetsky, V.; Graham, I.; Zellmer, G.; Dziak, R.; Embley, R.; Dekov, V.; Munnik, F.; Lahr, J.; Evans, L.; Takai, K. Submarine hydrothermal activity and gold-rich mineralization at Brothers Volcano, Kermadec Arc, New Zealand. *Miner. Deposita*. **2011**, 46(5), 541-584.
38. Vaughan, D.J.; Rosso, K.M. Chemical bonding in sulfide minerals. *Reviews in Mineralogy and Geochemistry.* **2006**, 61, 231-264.
39. Maslennikov, V.V.; Maslennikova, S.P.; Large, R.R.; Danyushevsky, L.V. Study of trace element zonation in vent chimneys from the Silurian Yaman-Kasy volcanic-hosted massive sulfide deposit (Southern Urals, Russia) using laser ablation-inductively coupled plasma mass

Preprints (www.preprints.org) | NOT PEER-REVIEWED | Posted: 4 September 2018 doi:10.20944/preprints201809.0064.v1

Peer-reviewed version available at Minerals 2018, 8, 526; doi:10.3390/min8110526

spectrometry (LA-ICPMS). *Econ. Geol.* **2009**, 104, 1111-1141.

40. Maslennikov, V.V.; Maslennikova, S.P.; Large, R.R.; Danyushevsky, L.V. Study of Trace Element Zonation in Vent Chimneys from the Silurian Yaman-Kasy Volcanic-Hosted Massive Sulfide Deposit (Southern Urals, Russia) Using Laser Ablation-Inductively Coupled Plasma Mass Spectrometry (LA-ICPMS). *Econ. Geol.* **2009**, 104(8), 1111 -1141.
41. Auclair, G.; Fouquet, Y.; Bohn, M. Distribution of selenium in high-temperature hydrothermal sulfide deposits at 13° North, East Pacific Rise. *Can. Mineral.* **1987**, 25, 577-587.
42. Hannington, M.D.; Herzig, P.M.; Scott, S.D.; Thompson, G.; Rona, P.A. Comparative mineralogy and geochemistry of gold-bearing sulfide deposits on the mid-ocean ridges. *Mar. Geol.* **1991**, 101, 217-248.
43. Halbach, P.; Fouquet, Y.; Herzig, P. Mineralization and compositional patterns in deep-sea hydrothermal systems. In *Energy and mass transfer in marine hydrothermal systems*; Tunnicliffe, V., Hein, J.R, Eds.; Dahlem University Press: Berlin, Germany, 2003, pp. 85-122.
44. Cook, N.J.; Ciobanu, C.L.; Mao, J. Textural control on gold distribution in As-free pyrite from the Dongping, Huangtuliang and Hougou gold deposits, North China Craton (Hebei Province, China). *Chem. Geol*. **2009**, 264, 101-121.
45. Keith, M.; Haase, K.M.; Schwarz-Schampera, U.; Klemd, R.; Petersen, S.; Bach, W. Effects of temperature, sulfur, and oxygen fugacity on the composition of sphalerite from submarine hydrothermal vents. *Geology.* **2014**, 42, 699-702.
46. Rosso, K.M.; Vaughan, D.J. Sulfide Mineral Surfaces. *Reviews in Mineralogy and Geochemistry*. **2006**, 61(1), 505-556.
47. Mozgova, N.N.; Trubkin, N.V.; Borodaev, Y.S.; Cherkashev, G.A.; Stepanova, T.V.; Semkova, T.A.; Uspenskaya, T.Y. Mineralogy of massive sulfides from the Ashadze hydrothermal field, 13°N, Mid-Atlantic Ridge. *Can. Mineral.* **2008**, 46, 545-567.
48. Melekestseva, I.Y.; Maslennikov, V.V.; Maslennikova, S.P.; Danyushevsky, L.V.; Large, R. Covellite of the Semenov-2 hydrothermal field (13°31.13′N, Mid-Atlantic Ridge): Enrichment in trace elements according to LA ICP MS analysis. *Dokl. Earth Sci.* **2017b**, 473(1), 291-295.
49. Cook, N.J.; Ciobanu, C.L.; Danyushevsky, L.V.; Gilbert, S. Minor and trace elements in bornite and associated Cu–(Fe)-sulfides: A LA-ICP-MS study Bornite mineral chemistry. *Geochim. Cosmochim. Acta* **2011**, 75, 6473-6496.
50. Houghton, J.L.; Shanks III, W.C.; Seyfried, Jr. W.E. Massive sulfide deposition and trace element remobilization in the Middle Valley sediment-hosted hydrothermal system, northern Juan de Fuca Ridge. *Geochim. Cosmochim. Acta.* **2004**, 68, 2863-2873.
51. Melekestseva, I.Y.; Zaykov, V.V.; Nimis, P.; Tret'Yakov, G.A.; Tessalina, S.G. Cu–(Ni–Co–Au)-bearing massive sulfide deposits associated with mafic–ultramafic rocks of the Main Urals Fault, South Urals: Geological structures, ore textural and mineralogical features, comparison with modern analogs. *Ore Geol. Rev.* **2013**, 52(0), 18-36.
52. Salters, V.J.M.; Stracke, A. Composition of the depleted mantle. *Geochem. Geophys. Geosyst.*

Preprints (www.preprints.org) | NOT PEER-REVIEWED | Posted: 4 September 2018 doi:10.20944/preprints201809.0064.v1

Peer-reviewed version available at *Minerals* **2018**, *8*, 526; doi:10.3390/min8110526

2004, 5(5), Q5B-Q7B.

53. White, W.M.; Klein, E.M. Composition of the Oceanic Crust. In *Treatise on Geochemistry* 2nd ed.; Holland, H.D., Turekian, K.K. Eds; Elsevier: Oxford, 2014, pp. 457-496.
54. Melekestseva, I.Y.; Tret'Yakov, G.A.; Nimis, P.; Yuminov, A.M.; Maslennikov, V.V.; Maslennikova, S.P.; Kotlyarov, V.A.; Beltenev, V.E.; Danyushevsky, L.V.; Large, R.R. Barite-rich massive sulfides from the Semenov-1 hydrothermal field (Mid-Atlantic Ridge, 13°30.87′N): Evidence for phase separation and magmatic input. *Mar. Geol.* **2014**, 349, 37-54.
55. Arevalo, R.; McDonough, W.F. Chemical variations and regional diversity observed in MORB. *Chem. Geol.* **2010**, 271, 70-85.
56. Hannington, M.D.; Tivey, M.K.; Larocque, A.C.L.; Petersen, S.; Rona, P.A. The occurrence of gold in sulfide deposits of the TAG hydrothermal field, Mid-Atlantic Ridge. *Can. Mineral.* **1995**, 33, 1285-1310.
57. Bogdanov, Yu.A.; Lein, A.; Maslennikov, V.; Li, S.; Ul'yanov, A. Mineralogical-geochemical features of sulfide ores from the Broken Spur hydrothermal vent field. *Oceanology* **2008**, 48, 679-700.
58. Okino, K.; Nakamura, K.; Sato, H. Tectonic background of four hydrothermal fields along the Central Indian Ridge. In *Subseafloor Biosphere Linked to Hydrothermal Systems: TAIGA Concept*; Ishibashi, J., Okino, K., Sunamura, M., Eds.; Springer: Tokyo Japan 2015, 133-146.
59. Ryan, W.B.F.; Carbotte, S.M.; Coplan, J.O.; O'Hara, S.; Melkonian, A.; Arko, R.; Weissel, R.A.; Ferrini, V.; Goodwillie, A.; Nitsche, F.; Bonczkowski, J.; Zemsky, R. Global Multi-Resolution Topography synthesis. *Geochem. Geophys. Geosys t.* **2009**, 10(3), Q03014.